ADVANCED FUNCTIONAL MATERIALS
www.afm-journal.de

An Optimized and General Synthetic Strategy for Fabrication of Polymeric Carbon Nitride Nanoarchitectures

*Jinshui Zhang, Fangsong Guo, and Xinchen Wang**

Nanostructured covalent carbon nitride (CN) holds great promise for artificial photosynthesis, but its nanotexturation using templating methods is restricted by the weak binding affinities of neutral silica templates towards basic precursors that are kinetically difficult to diffuse into the nanopores of the templates. This weak affinity leads to an incomplete inclusion of the CN precursors into the nanostructured silica templates, and consequently, yields a defective replica of the parent porous structures. Here, this issue is addressed through the development of an innovative synthetic strategy to facilitate the sufficient inclusion of CN precursors in silica templates, by taking advantage of the surface acidification of silica and sonication-promoted insertion. The ordered mesoporous CN (ompg-CN) fabricated using SBA-15 mesozeolite as the template has been demonstrated to show a better 2D mesoporous hexagonal framework, larger surface area, and higher photocatalytic activity than that synthesized by the traditional method. This innovative strategy can in general be expanded to other silica templates with various nanostructures, enabling the creation of stable polymeric CN nanostructures with maximized material and structure functions.

1. Introduction

The synthesis and characterization of semiconductor nanostructures have for many years attracted great attention, owing to unique structure-dependent properties of such nanostructures that enable their potential applications in sensors, (photo) catalysis, optoelectronics, as supports, nanodevices, and so on.[1] When functioning as photocatalysts, the nanostructured materials exhibit a better performance for solar-driven chemical conversions than their corresponding bulk counterparts, due to the surface, interface, and photon effects that interact cooperatively to facilitate mass diffusion, light absorption, and long-range charge separation.[2] Until now, various kinds of nanostructures have been developed for inorganic semiconductors with controlled shape (e.g., rods, sheets, and spheres) and dimension on the nano-, micro-, and macroscales by chemical and physical protocols, such as sol-gel processing, hard/soft template synthesis, hydrothermal/solvothermal methods, and self-assembly.[3] In contrast to the easy morphology control of inorganic semiconductors, the construction of stable organic/polymeric complex nanostructures is relatively less successful, because of the "soft" nature of organic systems that appear to be highly vulnerable to macrostructural collapse/deformation after the removal of hard templates or solvents, especially under a thermal driving force.[4] Nevertheless, the emerging applications of organic/polymeric semiconductors as active elements in opto-related applications (e.g., photocatalysis or optoelectronic devices), together with their inherent advantages such as easy chemical modification, mechanical flexibility, and low cost, motivate enormous interest in the textural engineering of nanoarchitecture of π-conjugated semiconductors, by taking advantage of unique nanostructure-dependent photophysical and chemical properties.[5]

Recently, a poly(tri-*s*-triazine) based CN organic semiconductor with a visible-light-driven bandgap and proper band positions, has been widely used as a metal-free energy transducer for the sustainable utilization of solar energy for relevant chemical reactions, including water reduction/oxidation, electricity generation, organic photosynthesis, and environmental remediation.[6–9] However, the photocatalytic activities of pristine CN are seriously limited by intrinsic drawbacks originating from the π-conjugated system and its relatively low surface area, in particular, fast charge recombination and poor mass diffusion/transfer.[10] Hence, the development of physical, chemical, or combined protocols to modify CN solids with optimized textural, electronic, and optical properties to promote photochemical reactions has become a rather urgent necessity to advance carbon nitride photocatalysis.[11]

Control of the CN nanostructure matrix to endow the materials with desired surface properties and morphologies has already been demonstrated as a successful and efficient pathway to promote charge migration and separation, as well as the mass diffusion/transfer during photoredox reactions, greatly enhancing the photocatalytic performance.[12] Various kinds of CN-based nanoarchitectures, such as ordered mesoporous CN (ompg-CN), CN spheres, and CN nanorods, have been synthesized with the aid of sacrificial templates, particularly silicas.[13] However, the traditional method (as elucidated

J. Zhang, F. Guo, Prof. X. Wang
Research Institute of Photocatalysis
Fujian Provincial Key Laboratory
of Photocatalysis-State Key Laboratory Breeding Base
and College of Chemistry and Chemical Engineering
Fuzhou University
Fuzhou 350002, P. R. China
E-mail: xcwang@fzu.edu.cn

DOI:10. 1002/adfm.201203287

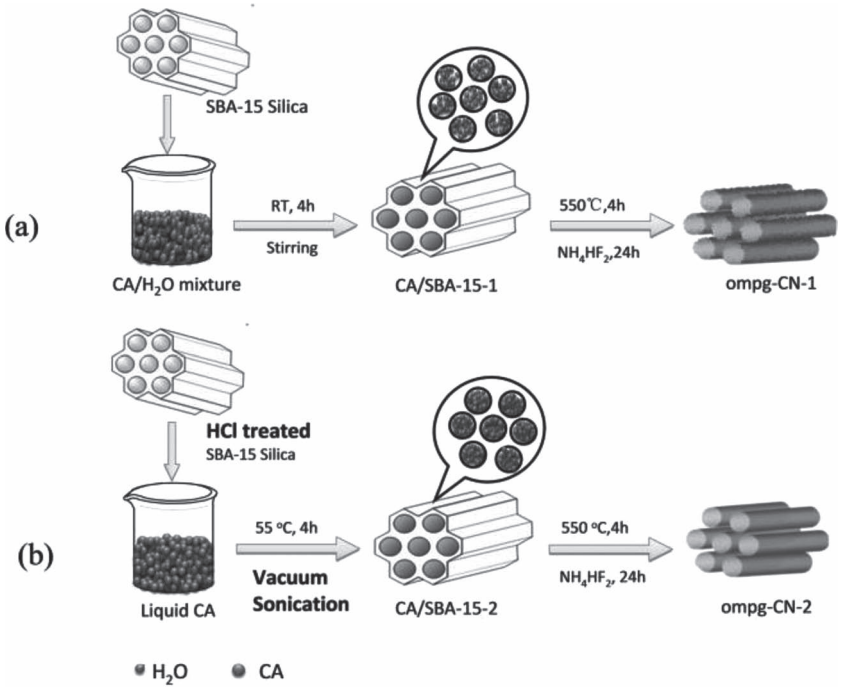

Scheme 1. Illustration for the synthesis process of ompg-CN using a) traditional method and b) new method.

in **Scheme 1**a) used for the nanostructural engineering of poly(tri-*s*-triazine) based CN matrix suffers from poor mass diffusion of organic precursors in the nanochannels of the templates, because the air trapped in the porous template greatly prevents the inclusion of organic molecules, making the complete infiltration of precursors into the structure-directing template very difficult.[13] In addition, the presence of H_2O or other solvents in starting materials often causes competitive absorption with precursor molecules on the templates. Thus, considerable textural structure defects or volume shrinkage are always induced after the removal of hard templates, which makes the morphology control of CN fine nanoarchitectures difficult.

Clearly, to address these issues, it is desirable to explore a new synthetic strategy that can effectively remove the air previously trapped by templates to accelerate the diffusion of organic precursors, as well as to avoid the competitive absorption caused by solvents. However, the wide use of easy-removal solvents (e.g., H_2O or ethanol) in starting materials greatly restricts the development of helpful techniques to extract absorbed air, because the solvents may be easier to remove than air due to their low boiling point and/or high saturated vapor pressure.[14] Development of a solvent-free synthesis approach is therefore becoming more and more urgent. Very recently, Zhao and coworkers used liquid cyanamide (CA) as an alternative precursor to a CA/H_2O mixture for the templated synthesis of ompg-CN, which provides a promising solution that avoids the competitive absorption between CA and H_2O.[15] Unfortunately, mass diffusion is still poor, and even more serious, because of the relative high viscosity and the rather low mobility of liquid CA.[16] Furthermore, the lack of chemical interaction between the silica and CA is also considered to be detrimental to the nanotemplating technologies. Thus, there is still evident collapse of ordered mesostructure and large shrinkage of wall matrix.[15]

Herein, an optimized and general synthetic strategy (Scheme 1b) focused on promoting the mass diffusion/transfer of liquid CA precursor in host nanospaces and also enhancing the chemical interaction between host and guest is developed for the fabrication of CN-based hierarchical nanoarchitectures. In the case of synthesizing ompg-CN, we employed the most easily available nanoporous SBA-15 silica as model template to elucidate the coupling effect of surface acidification and ultrasound-driven insertion.

In Scheme 1b, SBA-15 silica is post-acidified with dilute HCl (1 M) to enhance the surface reactivity of the silica towards NH_2-rich CA molecules via the chemical acid–base interaction. Then, by taking advantage of the relatively low saturated vapor pressure (0.067 KPa at 83 °C) of liquid CA,[16] a combined technology of sonication and vacuum is applied to extract the air trapped in the silica matrix, as well as to pump the CA molecules into the pore channels simultaneously via the bubble-collapsing effect, which leads to complete inclusion of SBA-15 silica and sufficiently filled mesochannels.[17] Finally, the obtained CA/SBA-15 mixture is transferred to an N_2 oven for thermal production of CN/SBA-15. After being etched by NH_4HF_2 solution, the resultant sample is denoted as ompg-CN-2, while that prepared via the traditional method is named as ompg-CN-1 and used as the reference. Detailed description of the syntheses of ompg-CN-1 and ompg-CN-2 is provided in the Experimental Section. The obtained ompg-CN-1 and ompg-CN-2 samples are carefully examined by physical analyses to investigate their morphology, texture, and optical and electronic properties. Their visible-light driven photocatalytic performance towards hydrogen evolution is also described to highlight the importance of well-developed nanoporous structures in supporting photocatalysis.

2. Results and Discussion

To demonstrate that innovative synthetic strategy can efficiently help to promote the inclusion of CA molecules in SBA-15 nanochannels, CA/SBA-15 and CN/SBA-15 prepared by two different methods (illustrated in Scheme 1) was subjected to thermogravimetric analysis (TGA) to ascertain the amount of CA or CN loaded on SBA-15 silica via the complete combustion of the organic species at high temperature.[13a] In **Figure 1**a,b, the mass loss increases with increased temperature, as CA or CN decompose to carbon- and nitrogen-containing gases. When the temperature reaches 800 °C, the final weight loss of CA/SBA-15-2 and CN/SBA-15-2 is calculated as 63.1% and 47.7%, respectively, much greater than 49.2% and 32.6% for CA/SBA-15-1 and CN/SBA-15-1. Hence, many more CA molecules are effectively included in SBA-15 nanotemplates via the new

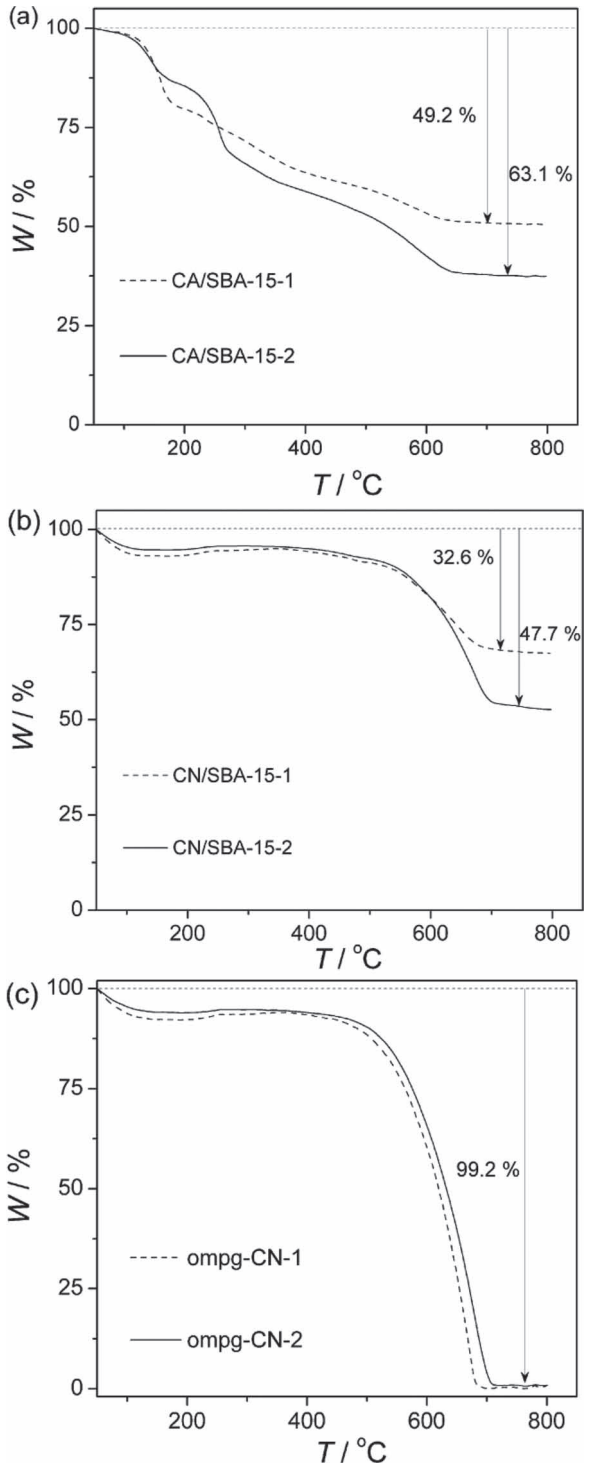

Figure 1. TGA curves of a) CA/SBA-15, b) CN/SBA-15, and c) ompg-CN.

method, because the coupling effect of surface acidification and ultrasonic-driven insertion can greatly accelerate the mass diffusion of CA precursors.

The silica templates in the CN/SBA-15 mixture were then removed by etching with NH_4HF_2 solution, and the resultant

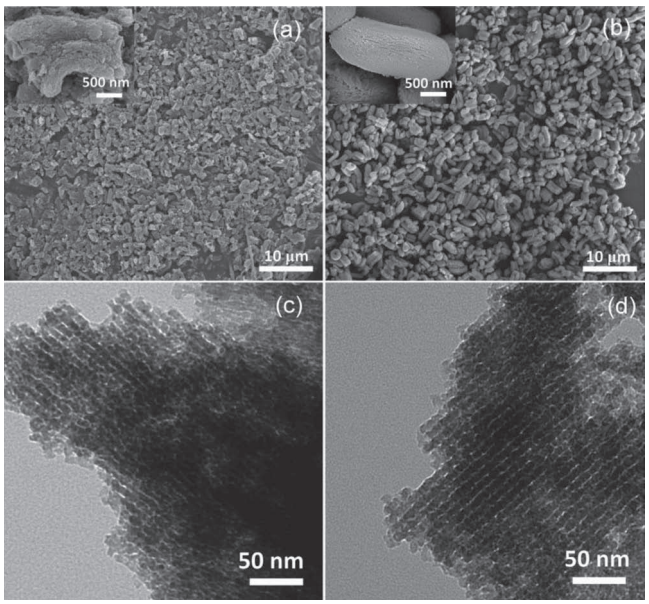

Figure 2. Typical SEM and TEM images of a,c) ompg-CN-1 and b,d) ompg-CN-2.

samples were also characterized using TGA. Figure 1c shows that only a little residue (<1.0 wt%) could be detected when the temperature increased to 800 °C, which suggests the successful removal of the silica template by NH_4HF_2 etching.[13] In addition, a better thermal stability against air is observed for ompg-CN-2, owing to its better organized textural framework and reduced textural structure defects.[6e,11e]

The morphology and textural structure of ompg-CN were investigated by using scanning electron microscopy (SEM) and transmission electron microscopy (TEM). In **Figure 2**a, serious large-scale texture deformation is observed for ompg-CN-1 after the removal of the silica templates, which reveals the disadvantage of the traditional method for organic/polymeric nanostructure construction. This structure collapse can be well suppressed by the alternative method to promote the diffusion of CA precursors (Scheme 1b). As demonstrated in Figure 2b, the rodlike morphologies of SBA-15 templates are faithfully replicated in the ompg-CN-2 framework, even to the regular surface intervals in an orderly fashion.[13] This improved textural framework is further evidenced by the TEM images in Figure 2c,d. For ompg-CN-2, the linear arrays of mesochannels along [100] direction are observed as arranged in an orderly, regular pattern, whereas a much less organized mesoporous structure with a considerable number of defects is detected for ompg-CN-1. The corresponding pore diameter of nanochannels, as indicated by the bright lines passing through the CN matrix, is calculated as about 5 nm for ompg-CN-1 and about 3 nm for ompg-CN-2, respectively. These values are comparable to the wall thickness (ca. 2 nm) of the parent SBA-15 silica,[13a] which suggests that the generation of ompg-CN architectures using the nanocasting method is indeed a process of negative replication, in which the nanochannels and their corresponding walls are created by the removal of silica walls and the thermal condensation of CA-filled-in silica channels, respectively.[13d] In addition, the smaller wall thickness in ompg-CN-2 indicates that the structure

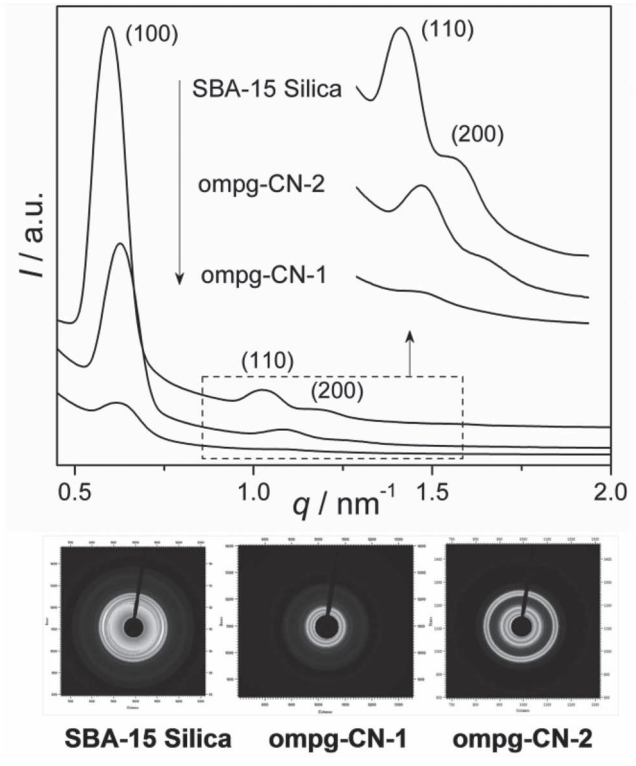

Figure 3. SAXS patterns of ompg-CN and SBA-15 silica, together with their corresponding 2D SAXS images.

shrinkage of the CN matrix is partly suppressed, which underlines the advantages of this new synthetic methodology for the fabrication of CN-based hierarchical architectures.

The mesostructural order of ompg-CN was further examined by using small-angle X-ray scattering (SAXS) measurements. As a result of negative replication, three distinct peaks, assigned to the (100), (110), and (200) reflections of the highly ordered 2D hexagonal mesostructure with a *p6mm* symmetry, are clearly inherited from SBA-15 silicas into ompg-CN frameworks (**Figure 3**).[13] However, a considerably broader diffraction of the *p6mm* space group with reducing intensity is observed for ompg-CN-1, which suggests it has less mesostructural order of 2D hexagonal frameworks than does ompg-CN-2. The corresponding unit-cell constants of ompg-CN, together with the value for SBA-15, are summarized in **Table 1**.

More detailed information about the ordered framework of ompg-CN was accessed by making use of nitrogen absorption–desorption isotherms. In **Figure 4**, a typical IV isotherm

Table 1. Physical properties and photocatalytic performance of SBA-15 silica and ompg-CN.

Sample	d_{100} [nm]	a[a)] [nm]	SA[b)] [$m^2 g^{-1}$]	PV[c)] [$cm^3 g^{-1}$]	PD[d)] [nm]	HER[e)] [$\mu molh^{-1}$]
SBA-15 silica	10.57	12.21	531	1.41	10.6	0
ompg-CN-1	10.05	11.60	234	0.32	5.2	141
ompg-CN-2	10.04	11.59	517	0.49	3.4	243

[a)]Unit cell parameter; [b)]surface area; [c)]pore volume; [d)]pore diameter; [e)]H_2 evolution rate.

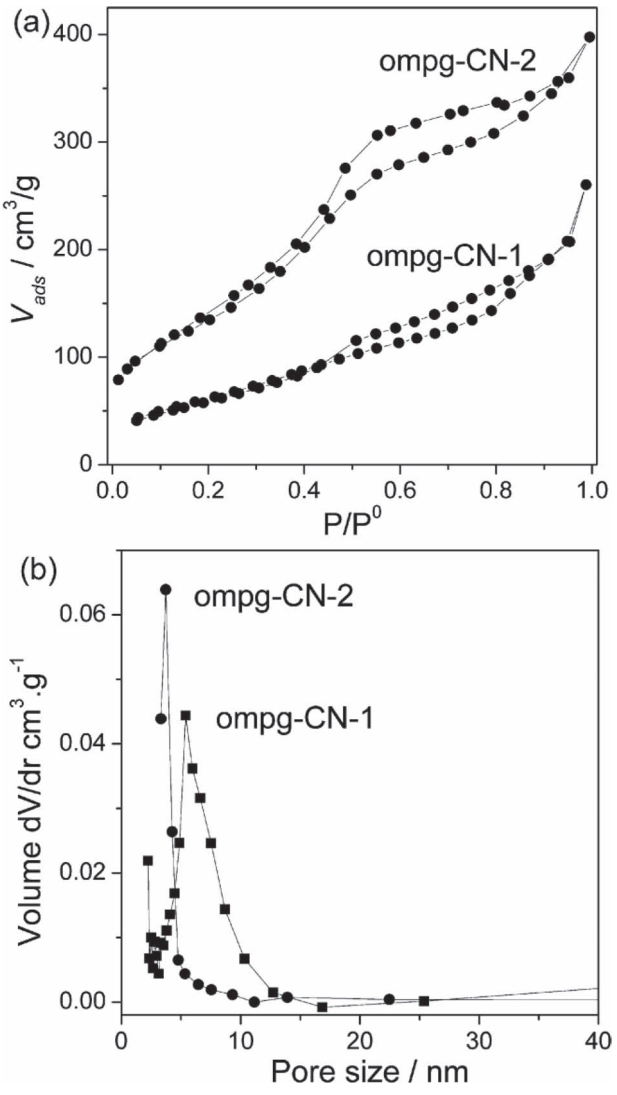

Figure 4. a) N_2-sorption isotherms and b) corresponding BJH pore-size distribution of ompg-CNs.

featuring an evident H1 hysteresis loop is observed for both ompg-CN-1 and ompg-CN-2; these indicate the successful creation of ordered mesopores and cylindrical channels in the CN matrix after the removal of the silica templates.[13c–e] As expected, ompg-CN-2 possesses a much higher specific surface area (517 $m^2 g^{-1}$) and correspondingly larger pore volume (0.49 $cm^3 g^{-1}$) than that of ompg-CN-1 (234 $m^2 g^{-1}$ and 0.32 $cm^3 g^{-1}$), because the new synthetic protocol can effectively promote the inclusion of CA precursors to produce a better 2D mesoporous hexagonal framework (Scheme 1b). In addition, another advantage of this novel synthetic approach is that the large shrinkage of wall matrix can be well suppressed, as clearly demonstrated by the smaller Barrett-Joyner-Halenda (BJH) pore size of ompg-CN-2 and its narrower distribution. Textural parameters calculated from nitrogen absorption–desorption isotherms are also listed in Table 1.

The physicochemical properties of the CN polymeric matrix were further characterized by means of wide-angle X-ray

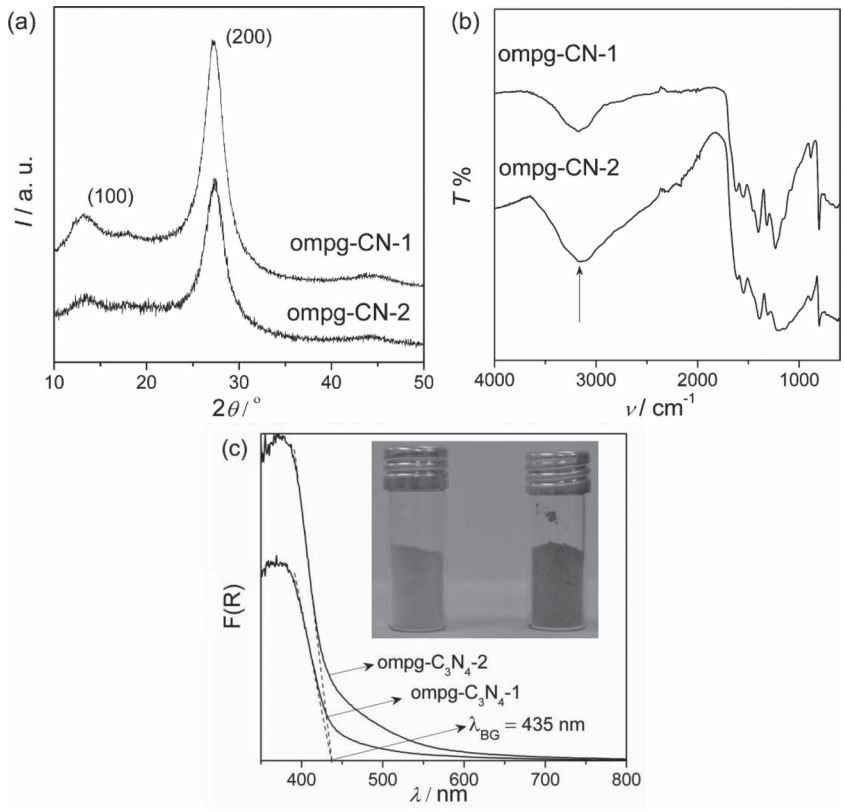

Figure 5. a) WA-XRD patterns, b) FT-IR spectra, and c) UV-Vis DRS spectra of ompg-CN. Inset in (c) is a photograph of ompg-CN-1 (left) and ompg-CN-2 (right).

diffraction (WA-XRD) patterns, Fourier-transformed infrared (FT-IR) spectra, and UV-Vis diffuse reflectance spectra (UV-Vis DRS). In **Figure 5**a, two individual well-resolved XRD reflections can be determined at 27.4° for (002) reflection and 13.0° for (100) reflection, which indicate that the characteristic graphitic-like layered stacking of CN-based materials is still retained after textural engineering using the SBA-15 nanotemplates.[6] According to Bragg's law, the corresponding *d*-spacing values of the (002) layered structure and (100) in-plane repeated units are 0.326 and 0.681 nm, respectively. In addition, owing to the reduced correlation length of interlayer periodicity of the CN motifs caused by the larger specific surface area and bigger pore volume, a considerably broader XRD reflection with reducing intensity is indeed observed for ompg-CN-2.[13d]

Figure 5b displays the FT-IR spectra of the ompg-CN samples, where typical vibration bonds assigned to CN-based polymers are clearly seen. The absorption band in the region of 1200 and 1600 cm^{-1} is a strong indication of the CN heterocycles, whereas the sharp peak at 802 cm^{-1} is caused by the breathing vibration of the triazine units.[11] Another evident absorption peaking at 3200 cm^{-1} is assigned to the free amino groups (e.g., $-NH_2$ or –NH) on the surface of the CN-based polymer. Note that ompg-CN-2 demonstrates a much stronger absorption at 3200 cm^{-1} than is the case for ompg-CN-1, owing to its enlarged surface area that exposes more surface uncondensed amino groups.[6,11] It is interesting that the presence of many more amino groups in 2D hexagonal nanochannels can potentially enable ompg-CN-2 to act as a green energy storage material for H_2 or CO_2 absorption,[13e,15] or to be functionalized as a promising platform for the controllable generation of nanoparticles, for example, Au nanoparticles.[18]

The optical absorption and energy bandgap of ompg-CN samples were examined by using UV-Vis DRS measurements. In Figure 5c inset, ompg-CN-2 displays a much deeper color over ompg-CN-1. The absorption threshold of both ompg-CN-1 and ompg-CN-2 samples have the same value of $\lambda_{BG} = 435$ nm (Figure 5c), which corresponds to a semiconductor bandgap of $E_{BG} = 2.85$ eV. Thus, the explanation of decreased bandgap energy to improve optical absorption can be excluded. According to a previous study,[12a,13a] this deeper color of ompg-CN-2 should be attributed to the nanostructure effect, because the enlarged surface area and the well-developed ordered mesochannels are both beneficial for multiple reflections of incident light.[12,19]

One of the promising applications of semiconductive CN nanoarchitectures is that they can function as metal-free photocatalysts for hydrogen production. Herein, ompg-CN-1 and ompg-CN-2 were tested for the photocatalytic generation of H_2 with visible light irradiation in a top-irradiation closed-circulation system, using in situ photodeposited Pt nanoparticles as the cocatalysts. In **Figure 6**, the produced H_2 gas linearly increases with duration of light irradiation, strongly demonstrating the visible-light-driven catalytic process of water reduction. Under 5 h consecutive

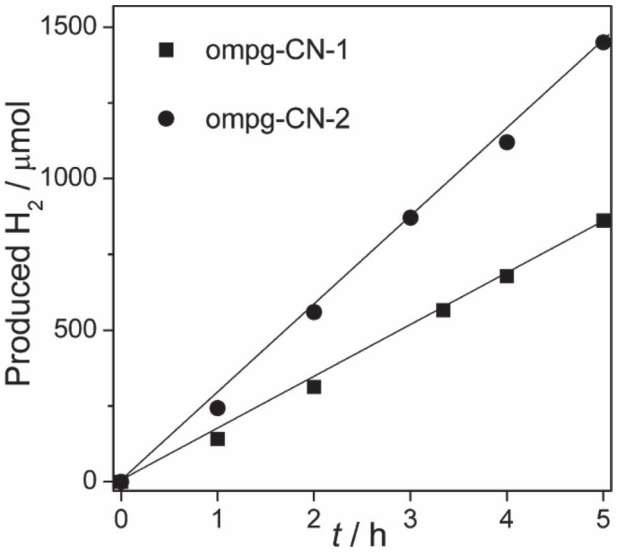

Figure 6. H_2-evolution by ompg-CN as a function of reaction time under visible-light irradiation ($\lambda > 420$ nm), using Pt nanoparticles as cocatalyst.

irradiation, the total amount of H_2 produced reaches 860 and 1450 μmol for ompg-CN-1 and ompg-CN-2, respectively, which corresponds to turnover numbers (TON) of 287 and 483 (based on Pt atoms).The apparent quantum yield (AQY) for H_2 evolution was also calculated for the ompg-CN photocatalysts. In Figure S3 (Supporting Information), the AQY values for ompg-CN-2 and ompg-CN-1 at 455 nm are estimated as 6.77% and 2.96%, respectively. This better photocatalytic performance for ompg-CN-2 should be attributed to the improved order of mesochannels, the presence of fewer textural structure defects, and, finally, the larger specific surface area. The improved textural structure, especially the well-organized 2D hexagonal frameworks, can function as a "highway" for free-charge transport to reduce the energy-wasteful electron–hole recombination, and hence promote photoredox functions.

3. Conclusions

In summary, an optimized and general synthetic strategy aim to accelerate the diffusion of CA precursors has been successfully established for the templated construction of CN-based nanoarchitecture. As demonstrated by the case study of ompg-CN synthesis, surface acidification and sonication-promoted insertion technologies can work together to sufficiently tune the surface reactivity of the silica matrix and effectively remove the air trapped in nanochannels. Both of these protocols facilitate the infiltration of CA precursors into the SBA-15 templates, and thus, greatly improve the mesostructural perfection of ompg-CN. The optimized ompg-CN exhibits an enhanced photocatalytic activity towards hydrogen evolution over that synthesized by the traditional method. One can expect the extension of the current synthetic method to the construction of various kinds of CN-based nanoarchitectures, by using complex structured silica templates with very small pore diameters or narrow channels.

4. Experimental Section

Materials: Pluronic P123 (M_w = 5800), tetraethylorthosilicate (TEOS, 98%), HCl (37%), cyanamide (CA, 99%), triethanolamine (99%), $H_2PtCl_6.6H_2O$ (≥37.5% Pt basis), NH_4HF_2 (95%) were purchased from Sigma-Aldrich. All chemicals were used as-received, without further purification.

SBA-15 Silica: SBA-15 silica was obtained using Pluronic P123 and TEOS as the starting materials, according to the method reported.[13a] In a typical preparation, TEOS (5.58 g) was mixed with P123 (3.46 g) in 1.6 M HCl solution (38 mL) and stirred at 35 °C for 24 h. The mixture was heated at 150 °C for 24 h in static conditions in a Teflon-lined autoclave. The resulting white precipitate was removed by filtration and dried at 80 °C overnight; it was then further calcined at 550 °C in air for 4 h with a heating rate of 1 °C min^{-1}. For information about the characterization of SBA-15 silica, see Figure S1 in theSupporting Information.

ompg-CN-1: In a typical synthesis, 1.0 g SBA-15 silica was impregnated in 22.5 mL water containing 8 g CA, and kept stirring at room temperature for 4 h. Then, the resultant mixture was centrifuged, dried, and finally calcined at 550 °C for 4 h. The obtained powder was treated with 4 M NH_4HF_2 solution (40 mL) for 24 h to remove the silica template, followed by filtration, washing with water and ethanol several times, and finally drying at 80 °C.

ompg-CN-2: First, the as-prepared SBA-15 silica was acidified using 1 M HCl solution (1.0 g silica/20.0 mL HCl) at 80 °C for 24 h, followed by drying at 80 °C for 12 h. Then, 1.0 g HCl-treated SBA-15 silica was added to 8 g liquid CA, and kept under sonication and vacuum at 55 °C for 4 h. Third, 15.0 mL water was added to the mixture, which was then centrifuged, dried, and calcined at 550 °C for 4 h. The resulting powder was treated with 4 M NH_4HF_2 solution (40 mL) for 24 h to remove the silica template, followed by filtration, washing with water and ethanol several times, and finally drying at 80 °C.

Characterization: TGA was performed on an STA 449 F3 (NETZSCH Co.) The sample picture was taken with a Nikon D 3100. SEM and TEM images were obtained by using a Nova Nano 230 microscope and Zeis 912 microscope, respectively. SAXS measurements were carried out using a Nonius rotating anode (Cu Kα radiation, λ = 1.5406 Å) with pinhole collimation and a MAR CCD area detector (sample–detector distance of 740 mm). WA-XRD measurements were performed on a Bruker D8 Advance diffractometer with Cu$K\alpha_1$ radiation (λ = 1.5406 Å). FT-IR spectra were recorded on a BioRad FTS 6000 spectrometer. Nitrogen adsorption–desorption isotherms were collected at 77 K using a Micromeritics ASAP 2020 Surface Area and Porosity Analyzer. UV-Vis diffuse reflectance spectra (UV-Vis DRS) were recorded on a Varian Cary 500 Scan UV-visible system.

Photocatalytic Activity for Water Splitting: Reactions were carried in a Pyrex-top irradiation reaction vessel connected to a glass closed gas system. H_2 was produced by dispersing 20 mg catalyst in an aqueous solution (100 mL), using triethanolamine (10 vol%) and 3 wt% Pt as electron donors and cocatalyst, respectively. The reaction solution was evacuated several times to remove air completely prior to irradiation under a 300 W xenon lamp. The wavelength of the incident light for H_2 evolution was controlled at $\lambda > 420$ nm with the aid of cut-off filters. The temperature of the reaction solution was maintained at 10 °C by a flow of cooling water during the reaction. The evolved gases were analyzed by gas chromatography equipped with a thermal conductive detector (TCD) and a 5 Å molecular sieve column, using argon as the carrier gas. The apparent quantum yield (AQY) for H_2 evolution was measured using a similar experimental setup, only with a 455-nm band-pass filter. The average intensity of irradiation was measured as 8.873 mW cm^{-2} (ILT 950 spectroradiometer) and the irradiation area was controlled at 10.14 cm^2. After 3 h irradiation, the produced H_2 molecules reached 54.7 and 125 μmol for ompg-CN-1and ompg-CN-2, respectively (Figure S3, Supporting Information). The AQY was estimated as:

$$\mathrm{AQY}(\%) = \frac{\text{number of reacted electrons}}{\text{number of incident photons}} \times 100 = \frac{\text{number of evolved } H_2 \text{ molecules} \times 2}{\text{number of incidents photons}} \times 100$$

Supporting Information

Supporting Information is available from the Wiley Online Libray or from the author.

Acknowledgements

This work was financially supported by the National Basic Research Program of China (2013CB632405), the National Natural Science Foundation of China (21033003 and 21173043), and the Department of Education of Fujian Province in China.

Received: November 9, 2012
Revised: December 2, 2012
Published online: January 16, 2013

[1] a) C. Burda, X. Chen, R. Narayanan, M. A. El-Sayed, *Chem. Rev.* **2005**, *105*, 1025–1102; b) P. D. Cozzoli, T. Pellegrino, L. S. Manna, *Chem. Soc. Rev.* **2006**, *35*, 1195–1208; c) M. Law, J. Goldberger, P. Yang, *Ann. Rev. Mater. Res.* **2004**, *34*, 83–122; d) P. Yang, Y. Zhao, Y. Lu, Q. Z. Xu, X. W. Xu, L. Dong, S. H. Yu, *ACS Nano* **2011**, *5*,

2147–2154; e) K. J. Moon, T. I. Lee, J. H. Choi, J. Jeon, Y. H. Kang, J. P. Kar, J. H. Kang, I. Yun, J. M. Myoung, *ACS Nano* **2011**, *5*, 159–164; f) R. Yan, D. Gargas, P. Yang, *Nat. Photonics* **2009**, *3*, 569–576.

[2] a) P. V. Kamat, *J. Phys. Chem. C* **2007**, *111*, 2834–2860; b) A. Takagaki, C. Tagusagawa, S. Hayashi, M. Hara, K. Domen, *Energy Environ. Sci.* **2010**, *3*, 82–93; c) P. Chen, T. Y. Xiao, H. H. Li, J. J. Yang, Z. Wang, H. B. Yao, S. H. Yu, *ACS Nano* **2012**, *6*, 712–719; d) K. Maeda, K. Domen, *Chem. Mater.* **2010**, *22*, 612–623; e) M. Feng, M. Zhang, J. M. Song, X. G. Li, S. H. Yu, *ACS Nano* **2011**, *5*, 6726–6735.

[3] a) J. C. Hulteen, C. R. Martin, *J. Mater. Chem.* **1997**, *7*, 1075–1087; b) Z. R. Dai, Z. W. Pan, Z. L. Wang, *Adv. Funct. Mater.* **2003**, *13*, 9–24; c) Y. Xia, P. Yang, Y. Sun, Y. Wu, B. Mayers, B. Gates, Y. Yin, F. Kim, H. Yan, *Adv. Mater.* **2003**, *15*, 353–389; d) Y. Jun, J. Choi, J. Cheon, *Angew. Chem. Int. Ed.* **2006**, *45*, 3414–3439; e) J. A. Rogers, *ACS Nano* **2007**, *1*, 151–153.

[4] G. L. Li, L. Q. Xu, X. Tang, K. G. Neoh, E. T. Kang, *Macromolecules* **2010**, *43*, 5797–5803.

[5] a) H. Xin, O. G. Reid, G. Ren, F. S. Kim, D. S. Ginger, S. A. Jenekhe, *ACS Nano* **2010**, *4*, 1861–1872; b) M. G. Schwab, M. Hamburger, X. Feng, J. Shu, H. W. Spiess, X. Wang, M. Antonietti, K. Müllen, *Chem. Commun.* **2010**, *46*, 8932–8934; c) A. F. Nogueira, C. Longo, M. A. Paoli, *Coord. Chem. Rev.* **2004**, *248*, 1455–1468.

[6] a) X. Wang, K. Maeda, A. Thomas, K. Takanabe, G. Xin, J. M. Carlsson, K. Domen, M. Antonietti, *Nat. Mater.* **2009**, *8*, 76–80; b) X. Wang, S. Blechert, M. Antonietti, *ACS Catal.* **2012**, *2*, 1596–1606; c) K. Maeda, X. Wang, Y. Nishihara, D. Lu, M. Antonietti, K. Domen, *J. Phys. Chem. C* **2009**, *113*, 4940–4947; d) J. Zhang, M. Grzelczak, Y. Hou, K. Maeda, K. Domen, X. Fu, M. Antonietti, X. Wang, *Chem. Sci.* **2012**, *3*, 443–446; e) J. Zhang, M. Zhang, G. Zhang, X. Wang, *ACS Catal.* **2012**, *2*, 940–948; f) Z. Lin, X. Wang, *Angew. Chem. Int. Ed.* **2012**, DOI: 10.1002/anie.201209017.

[7] Y. Zhang, A. Thomas, M. Antonietti, X. Wang, *J. Am. Chem. Soc.* **2009**, *131*, 50–51.

[8] a) F. Su, S. C. Mathew, L. Möhlmann, M. Antonietti, X. Wang, S. Blechert, *Angew. Chem. Int. Ed.* **2011**, *50*, 657–660; b) F. Su, S. C. Mathew, G. Lipner, X. Fu, M. Antonietti, S. Blechert, X. Wang, *J. Am. Chem. Soc.* **2010**, *132*, 16299–16301.

[9] Y. Cui, Z. Ding, P. Liu, M. Antonietti, X. Fu, X. Wang, *Phys. Chem. Chem. Phys.* **2012**, *14*, 1455–1462.

[10] a) A. Köhler, D. Santos, D. Beljonne, Z. Shuai, J. L. Brédas, A. B. Holmes, A. Kraus, K. Müllen, R. H. Friend, *Nature* **1998**, *392*, 903–906; b) J. Zhang, M. Zhang, R. Sun, X. Wang, *Angew. Chem. Int. Ed.* **2012**, *51*, 10145–10149; c) J. Zhang, G. Zhang, X. Chen, S. Lin, L. Möhlmann, G. Dołęga, G. Lipner, M. Antonietti, S. Blechert, X. Wang, *Angew. Chem. Int. Ed.* **2012**, *51*, 3183–3187; d) J. Zhang, J. Sun, K. Maeda, K. Domen, P. Liu, M. Antonietti, X. Fu, X. Wang, *Energy Environ. Sci.* **2011**, *4*, 675–678.

[11] a) H. Zheng, J. Zhang, X. Wang, X. Fu, *Acta Phys. Chim. Sin.* **2012**, *28*, 2336–2342; b) J. Zhang, X. Chen, K. Takanabe, K. Maeda, K. Domen, J. D. Epping, X. Fu, M. Antonietti, X. Wang, *Angew. Chem. Int. Ed.* **2010**, *49*, 441–444; c) G. Liu, P. Niu, C. Sun, S. C. Smith, Z. Chen, G. Q. Lu, H. M. Cheng, *J. Am. Chem. Soc.* **2010**, *132*, 11642–11648; d) N. Ping, L. Zhang, G. Zhang, H. Cheng, *Adv. Funct. Mater.* **2012**, *22*, 4763–4770; e) G. Zhang, J. Zhang, M. Zhang, X. Wang, *J. Mater. Chem.* **2012**, *22*, 8083–8091.

[12] a) X. Wang, K. Maeda, X. Chen, K. Takanabe, K. Domen, Y. Hou, X. Fu, M. Antonietti, *J. Am. Chem. Soc.* **2009**, *131*, 1680–1681; b) K. Kailasam, J. D. Epping, A. Thomas, S. Losse, H. Junge, *Energy Environ. Sci.* **2011**, *4*, 4668–4674; c) Y. Cui, J. Zhang, G. Zhang, J. Huang, P. Liu, M. Antonietti, X. Wang, *J. Mater. Chem.* **2011**, *21*, 13032–13039; d) H. Yan, *Chem. Commun.* **2012**, *48*, 3430–3432; e) J. Hong, X. Xia, Y. Wang, R. Xu, *J. Mater. Chem.* **2012**, *22*, 15006–15012.

[13] a) X. Chen, Y. S. Jun, K. Takanabe, K. Maeda, K. Domen, X. Fu, M. Antonietti, X. Wang, *Chem. Mater.* **2009**, *21*, 4093–4095; b) E. Z. Lee, Y. S. Jun, W. H. Hong, A. Thomas, M. M. Jin, *Angew. Chem. Int. Ed.* **2010**, *49*, 9706–9710; c) X. Jin, V. V. Balasubramanian, S. T. Selvan, D. P. Sawant, M. A. Chari, G. Q. Lu, A. Vinu, *Angew. Chem. Int. Ed.* **2009**, *48*, 7884–7887; d) S. N. Talapaneni, G. P. Mane, A. Mano, C. Anand, D. S. Dhawale, T. Mori, A. Vinu, *ChemSusChem* **2012**, *5*, 700–708; e) G. P. Mane, S. N. Talapaneni, C. Anand, S. Varghese, H. Iwai, Q. Ji, K. Ariga, T. Mori, A. Vinu, *Adv. Funct. Mater.* **2012**, *22*, 3596–3604; f) Q. Li, J. Yang, D. Feng, Z. Wu, Q. Wu, S. S. Park, C. S. Ha, D. Zhao, *Nano Res.* **2010**, *3*, 632–642; g) X. Li, J. Zhang, X. Chen, A. Fischer, A. Thomas, M. Antonietti, X. Wang, *Chem. Mater.* **2011**, *23*, 4344–4348.

[14] N. B. Keevil, *J. Am. Chem. Soc.* **1942**, *64*, 841–850.

[15] S. S. Park, S. W. Chu, C. Xue, D. Zhao, C. S. Ha, *J. Mater. Chem.* **2011**, *21*, 10801–10807.

[16] T. Güthner, B. Mertschenk, *Ullmann's Encyclopedia of Industrial Chemistry*, Wiley-VCH Verlag GmbH & Co. KGaA, Weinheim **2000**.

[17] J. C. Yu, X. C. Wang, L. Wu, W. K. Ho, L. Z. Zhang, G. T. Zhou, *Adv. Funct. Mater.* **2004**, *14*, 1178–1183.

[18] K. K. R. Datta, B. V. S. Reddy, K. Ariga, A. Vinu, *Angew. Chem. Int. Ed.* **2010**, *49*, 5961–5965.

[19] X. Wang, J. C. Yu, C. Ho, Y. Hou, X. Fu, *Langmuir* **2005**, *21*, 2552–2559.